

UNCOVERING MAGNETIC TURBULENCE IN YOUNG SUPERNOVA REMNANTS WITH POLARIZED X-RAY IMAGING

ANDREI M. BYKOV,¹ YURY A. UVAROV,¹ PATRICK SLANE,² AND DONALD C. ELLISON³

Accepted in ApJ July 2020

ABSTRACT

Observations of young supernova remnants (SNRs) in X-rays and γ -rays have provided conclusive evidence for particle acceleration to at least TeV energies. Analysis of high spatial resolution X-ray maps of young SNRs has indicated that the particle acceleration process is accompanied by strong non-adiabatic amplification of magnetic fields. If Fermi acceleration is the mechanism producing the energetic cosmic rays (CRs), the amplified magnetic field must be turbulent and CR-driven instabilities are among the most probable mechanisms for converting the shock ram pressure into the magnetic turbulence. The development and evolution of strong magnetic turbulence in the collisionless plasmas forming SNR shells are complicated phenomena which include the amplification of magnetic modes, anisotropic mode transformations at shocks, as well as the nonlinear physics of turbulent cascades. Polarized X-ray synchrotron radiation from ultra-relativistic electrons accelerated in the SNR shock is produced in a thin layer immediately behind the shock and is not subject to the Faraday depolarization effect. These factors open possibilities to study some properties of magnetic turbulence and here we present polarized X-ray synchrotron maps of SNR shells assuming different models of magnetic turbulence cascades. It is shown that different models of the anisotropic turbulence can be distinguished by measuring the predominant polarization angle direction. We discuss the detection of these features in Tycho's SNR with the coming generation of X-ray polarimeters such as *IXPE*.

Keywords: acceleration of particles — ISM: cosmic rays — galactic clusters — magnetohydrodynamics (MHD) — shock waves — turbulence

1. INTRODUCTION

The synchrotron interpretation of non-thermal radio emission from “radio stars” by Alfvén & Herlofson (1950), while not directly mentioning supernovae (SNe), gave observational support to the hypothesis by Baade & Zwicky (1934) that SNe are sources of Galactic cosmic rays (see e.g. Ginzburg & Syrovatskii 1964; Axford 1981; Amato 2014). Collisionless shocks produced by supersonic SN ejecta expanding into the interstellar medium, simultaneously accelerate charged particles by the diffusive shock acceleration (DSA) mechanism while amplifying the local turbulent magnetic field (for reviews, see Blandford & Eichler 1987; Schure et al. 2012; Marcowith et al. 2016). As a result, quasi-power law particle spectra are formed where a significant fraction of the total SN ejecta kinetic energy can be deposited in relativistic cosmic rays (CRs).

Electrons can be accelerated by fast shocks up to TeV energies and efficiently emit synchrotron radiation up to X-ray energies in the amplified magnetic fields (see e.g. Reynolds & Chevalier 1981). This model is supported by observations which confirm the existence of a power law component in nonthermal SNR radiation in a broad spectral range from radio to X-rays (see e.g. Helder et al.

2012).

Direct observations of polarized radio emission from SNRs proved the synchrotron nature of the radiation and provided a way to study the magnetic field structure (see Chevalier 1977; Raymond 1984; Reynolds et al. 2012; Dubner & Giacani 2015, for reviews). Radio mapping of the young SNRs Cas A (Bell et al. 1975) and Tycho (Strom & Duin 1973; Duin & Strom 1975; Dickel et al. 1991; Reynoso et al. 1997) resolved well-defined edges of the radio shells associated with the forward shock waves. This magnetic field structure revealed from radio observations in young SNRs is often characterized by predominantly radial fields, while older SNRs, like the Cygnus Loop, IC 443 and others, show a tangential magnetic field structure (e.g., Fürst & Reich 2004).

The nature of the apparent predominantly radial field is still under discussion. Recently, West et al. (2017) considered selection effects due to the distribution of CR electrons accelerated by quasi-parallel shocks as an explanation of the radial magnetic field pattern derived from radio polarization observations. The authors demonstrated that radio-emitting electrons accelerated at quasi-parallel shocks can have spatial distributions that result in an apparent radial magnetic field in radio synchrotron maps even when the field is in fact disordered. Bandiera & Petruk (2016) and Petruk et al. (2017) modeled radio images of SNRs accounting for turbulent magnetic fields.

Since GeV electrons, regardless of origin, have long lifetimes in the Galaxy, their synchrotron radio emission

¹ Ioffe Institute for Physics and Technology, 194021 St. Petersburg, Russia; byk@astro.ioffe.ru

² Harvard-Smithsonian Center for Astrophysics, Cambridge MA 02138, U.S.A.; slane@cfa.harvard.edu

³ Physics Department, North Carolina State University, Box 8202, Raleigh, NC 27695, U.S.A.; ellison@ncsu.edu

can be used to study large scale magnetic turbulence (Lee et al. 2019; Wang et al. 2020). The ubiquitous nature of radio emission in SNRs provides direct constraints on the injection and shock acceleration of GeV electrons, as well as propagation and polarization in turbulent magnetic fields (e.g., Lazendic et al. 2004; Reynolds 2008). Here, however, we limit discussion to polarized X-ray synchrotron radiation where the rapid energy loss of TeV electrons means they are restricted to a thin shell behind the remnant forward shock. In this case, the Faraday depolarization effects are negligible in X-rays contrary to the radio band observations.

This provides the opportunity to reach a degree of polarization detectable with the new generation of X-ray polarimeters such as the Imaging X-ray Polarimetry Explorer (*IXPE*) (Weisskopf et al. 2016).

The TeV electrons producing X-ray synchrotron emission in SNRs are likely accelerated by the DSA mechanism (e.g., Blandford & Eichler 1987; Ellison et al. 2012). This mechanism requires magnetic turbulence to function and, while pre-existing background turbulence is always present in astrophysical plasmas, locally generated broadband turbulence is necessary to produce GeV-TeV CRs. This turbulence is most likely produced in the shock precursor by instabilities generated by backstreaming CRs. Models show that these instabilities can transfer a few percent of the shock ram pressure to the magnetic field fluctuations (see e.g. Bell 2004; Amato & Blasi 2006; Schure et al. 2012; Bykov et al. 2014). The effect of turbulent magnetic fields on X-ray synchrotron images of young SNRs was discussed by Bykov et al. (2008, 2009).

High resolution *Chandra* X-ray synchrotron maps of young SNRs revealed a number of structures of different sizes and morphologies (Vink 2012). These included narrow filaments, stripes, and clumps (see e.g. Vink & Laming 2003; Bamba et al. 2005; Patnaude & Fesen 2009; Eriksen et al. 2011). It was also discovered that small scale structures were time-variable on a scale of a few years in the case of SNR RX J1713.72 (Uchiyama et al. 2007) Cas A (Uchiyama & Aharonian 2008), and Tycho (Okuno et al. 2020). It was argued that the filamentary structures might result from fast energy losses of the X-ray emitting TeV electrons downstream from the shock if the downstream field was amplified well above the adiabatic compression magnitude. If so, the filaments are due to the geometric projection of the thin regions accelerating the TeV electrons. An alternative explanation of the filaments is due to a rapid decay of amplified magnetic fields in the vicinity of the shock wave (Pohl et al. 2005).

The time-variable clumpy structure detected by *Chandra* can also be naturally explained as a result of turbulent magnetic fields in the vicinity of the shock front without postulating an exceptionally strong uniform background field or field decay (Bykov et al. 2008). In this model, the intensity and polarization of the structures are sensitive to the magnetic turbulence spectrum even in the case of isotropic turbulence (Bykov et al. 2009). The observational diagnostics of the isotropic

turbulence in SNRs will require arcsecond resolution polarimetry which could be available with the next generation of X-ray polarimeters.

However, as we show below, anisotropic turbulence in young SNRs can be tested with upcoming polarimeters like *IXPE*. Not only is broadband self-generated turbulence necessary to produce GeV-TeV CR electrons and ions, there is ample evidence, particularly from sharp X-ray synchrotron edges, that this turbulence can be amplified by orders of magnitude above background levels (e.g., Parizot et al. 2006). As this turbulence is compressed upon entering the downstream region, where most of the X-ray synchrotron radiation is produced, it should become highly anisotropic.⁴

In addition, the turbulence anisotropy may evolve due to MHD plasma evolution (Shebalin et al. 1983; Cho et al. 2002; Bigot et al. 2008; Reville et al. 2008), such as anisotropic wave cascading (Sridhar & Goldreich 1994; Goldreich & Sridhar 1997; Lithwick & Goldreich 2003). In this paper we consider both (i) anisotropic turbulence due to shock compression of isotropic precursor turbulence⁵ and (ii) the anisotropic turbulence emerging in a cascading process. These two scenarios produce turbulence with different characteristics that can be distinguished in SNR X-ray synchrotron maps.

2. MODELING OF SNR SYNCHROTRON X-RAY IMAGES

2.1. Turbulence cascade

The time evolution of a turbulent magnetized plasma is a nonlinear process. However, in some conditions, the complicated physics of this process can be described as an interaction of linear MHD waves. In Sridhar & Goldreich (1994) it was shown for weak turbulence (i.e., when the small scale turbulent fields are weaker than the large scale field) in incompressible magnetized fluids that the 3-Alfvén-wave interaction is absent and a 4-wave interaction leads to the generation of waves with higher perpendicular wave number k_{\perp} . A special turbulent spectrum is formed with energy density $Wd^3k = C(k_{\parallel})k_{\perp}^{-10/3}dk_{\parallel}k_{\perp}dk_{\perp}$. While the spectrum has a specific dependence on k_{\perp} , the dependence on k_{\parallel} is determined by the initial turbulence.

If energy is injected in turbulence on large scales then only small k_{\parallel} are present in the turbulent spectrum and the assumption $C(k_{\parallel}) \approx \text{const}$ can be used. If the initial turbulence is isotropic (i.e., $\langle \delta B_x^2 \rangle = \langle \delta B_y^2 \rangle = \langle \delta B_z^2 \rangle = \langle \delta B^2 \rangle / 3$) the evolved turbulence will have $\langle \delta B_{\parallel}^2 \rangle > \langle \delta B_{\perp}^2 \rangle / 2$, where $\langle \delta B_{\parallel}^2 \rangle$ is the mean square of the turbulent magnetic field component directed along the large scale magnetic field and δB_{\perp} is the transverse component of the turbulent field. This effect is a result of the evolution of Alfvénic waves polarized so their mag-

⁴ We note that ambient magnetic fields can be amplified by non-CR processes such as Raleigh-Taylor and Kelvin-Helmholtz instabilities and this may result in a net radial polarization behind the forward shock (e.g., Jun & Norman 1996).

⁵ In oblique shocks, where the large-scale magnetic field direction is oblique to the shock normal, the magnetic field component tangent to the shock front is increased upon shock compression.

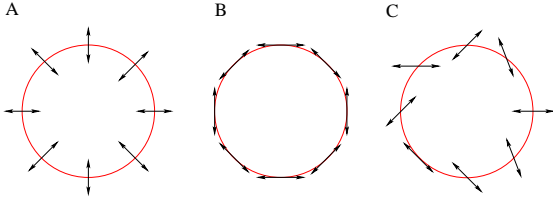


FIG. 1.— Sketch of SNR forward shock showing polarization directions immediately downstream. Example (A) shows the case of anisotropic turbulence produced by shock compression of upstream isotropic turbulence. Example (B) shows the case of turbulence produced by the anisotropic cascade of an almost radial magnetic field near the shock. Example (C) shows the domain structure formed from long-scale stochastic fluctuations of CR-driven magnetic turbulence produced by hard spectrum CRs in nonlinear DSA (see text).

netic field lies in the same plane as a wave vector and a large scale field. The existence of such polarization of Alfvén waves is a consequence of incompressibility.

In this work we consider three possible scenarios for polarization directions in supernova shells as sketched in Fig. 1. In (A) we show the case where there is strong, isotropic, short-scale turbulence in the shock precursor. Upon compression as the turbulence is swept across the shock, the magnetic field will become predominantly tangential to the shock front and the polarization will be predominantly radial. One should note that the nonlinear interactions of the fluctuations downstream from the shock may isotropise the tangential anisotropy induced by the transition through an oblique shock and reduce the degree of X-ray polarization. However, due to fast losses of TeV electrons the synchrotron X-ray radiation is formed in a thin ridge just behind the shock where the turbulence isotropization effect may be incomplete and significant X-ray polarization can be detected.⁶

In the case of anisotropic cascades (B), the predominant direction of the turbulent field is the same as the large-scale field. Since large-scale fields in young SNRs tend to be radial at the forward shock, synchrotron radiation will have a polarization direction predominantly tangent to the shock.

Our third case (C) assumes the CRs accelerated in the forward shock have a hard enough spectrum so strong, long-wavelength fluctuations on spatial scales up to 10 arcsec are produced in Tycho’s SNR. It should be noted here that even in the cosmic ray driven turbulence the long-wavelength fluctuations may have scales larger than the gyroradii of the highest energy cosmic rays if non-resonant instabilities like the firehose (see e.g. Schure et al. 2012; Bykov et al. 2013) or mirror instabilities (Bykov et al. 2017) are in operation. In this case, the magnetic field near the shock will form domains of this size with almost random field and polarization directions. The life-time of such long-scale fluctuations is longer than a year.

⁶ We illustrated both the fully anisotropic and fully isotropic cases in Fig. 4.

2.2. Numerical simulation of an anisotropic stochastic magnetic field

In a cascading process the direction of the large scale magnetic field defines the symmetry axis of the problem. The general stochastic property of axially symmetric magnetic turbulence is

$$\langle B_{\perp}^2 \rangle = q \langle B_{\parallel}^2 \rangle = \langle B^2 \rangle q / (q + 1) . \quad (1)$$

In the case of isotropic turbulence $\langle B_x^2 \rangle = \langle B_y^2 \rangle = \langle B_z^2 \rangle = \langle B^2 \rangle / 3$ and $q = 2$. For turbulence formed downstream from the shock by shock compression of initially isotropic turbulence $q > 2$, while $q < 2$ for turbulence produced in the cascading process described above.

For our simulation of anisotropic turbulence we use a method based on the work of Giacalone & Jokipii (1999). We consider the summation of a large number of harmonics with random wave vectors and phases:

$$\mathbf{B}(\mathbf{r}, t) = \sum_{n=1}^{N_m} \sum_{\alpha=1}^2 \mathbf{A}^{(\alpha)}(k_n) \cos(\mathbf{k}_n \cdot \mathbf{r} - \omega_n(\mathbf{k}_n) \cdot t + \phi_n^{(\alpha)}) \quad (2)$$

We have two orthogonal polarizations $\mathbf{A}^{(\alpha)}(k_n)$ ($\alpha = 1, 2$) of magnetic field, both chosen orthogonal to the wave vector $\mathbf{A}^{(\alpha)}(k_n) \perp \mathbf{k}_n$ in order to satisfy $\nabla \cdot \mathbf{B} = 0$. For the 1st polarization we choose the direction of the magnetic field to lie in a plane formed by the symmetry axis and the wave vector. The magnetic field direction for the 2nd polarization is orthogonal to this plane. We introduce here the coordinate system which is consisting of the axis \parallel directed along the symmetry axis and the perpendicular plane. The 2nd polarization gives contribution only to the value of B_{\perp} , while the 1st polarization contributes both to B_{\perp} and B_{\parallel} . The amplitudes for polarizations 1,2 are

$$A_1^2(\mathbf{k}) = (1 - a) A^2(\mathbf{k}) , \quad (3)$$

$$A_2^2(\mathbf{k}) = (1 + a) A^2(\mathbf{k}) , \quad (4)$$

where $a \geq -1$ and $q = (2 + a) / (1 - a)$. In the case of isotropic turbulence, the parameter $a = 0$ ($q = 2$) and the spectral energy density of the magnetic turbulence is

$$W d^3 k = C k^{-\delta} dk = 4\pi A^2(k) \cdot k^2 dk . \quad (5)$$

In the case of anisotropic turbulence produced by the shock compression of isotropic turbulence, we model the spectral energy density with the same expression with $a > 0$ ($q > 2$). For the anisotropic cascades considered by Sridhar & Goldreich (1994) the spectral energy density is

$$W d^3 k = C (k_{\parallel}) k_{\perp}^{-10/3} dk_{\parallel} k_{\perp} dk_{\perp} = 2\pi A^2(k) dk_z k_{\perp} dk_{\perp} . \quad (6)$$

2.3. Synchrotron radiation properties

A 2D SNR map is obtained by integrating a 3D distribution of synchrotron emissivity along each line-of-sight. We consider magnetic field fluctuations with characteristic sizes greater than the formation length

$l_f \approx mc^2/eH \approx 1.7 \times 10^9 B_{\mu G}^{-1}$ of the synchrotron radiation. This allows use of the standard formula for synchrotron radiation in a homogeneous magnetic field as given by Ginzburg & Syrovatskii (1965).

The Stokes parameters, \tilde{I} , \tilde{Q} , \tilde{U} , and \tilde{V} , that fully describe radiation polarization properties can be written as

$$\tilde{I}(\mathbf{r}, t, \nu) = S_c B_{\perp}(\mathbf{r}) \int_{\nu/\nu_c}^{\infty} K_{5/3}(\eta) d\eta, \quad (7)$$

$$\tilde{Q}(\mathbf{r}, t, \nu) = S_c B_{\perp}(\mathbf{r}) K_{2/3}\left(\frac{\nu}{\nu_c}\right) \cos(2\chi), \quad (8)$$

$$\tilde{U}(\mathbf{r}, t, \nu) = S_c B_{\perp}(\mathbf{r}) K_{2/3}\left(\frac{\nu}{\nu_c}\right) \sin(2\chi), \quad (9)$$

where $S_c = [\sqrt{3}e^3/(mc^2r^2)](\nu/\nu_c)$ and $\tilde{V} = 0$ for the isotropic particle distributions we consider here. These parameters are additive for incoherent photons so maps of Stokes parameters can be obtained by integration over the line-of-sight taking into account the distribution of emitting particles $f_e(E, \mathbf{r})$ and the expression $dV = r^2 dr d\Omega$:

$$I(\nu) = \int I(\nu, \mathbf{r}) dr = \quad (10)$$

$$\frac{\sqrt{3}e^3}{mc^2} \int dr dE \frac{\nu}{\nu_c} B_{\perp}(\mathbf{r}) f_e(E, \mathbf{r}) \int_{\nu/\nu_c}^{\infty} K_{5/3}(\eta) d\eta$$

$$Q(\nu) = \int Q(\nu, \mathbf{r}) dr = \quad (11)$$

$$\frac{\sqrt{3}e^3}{mc^2} \int dr dE \frac{\nu}{\nu_c} \cos(2\chi) B_{\perp}(\mathbf{r}) f_e(E, \mathbf{r}) K_{2/3}\left(\frac{\nu}{\nu_c}\right)$$

$$U(\nu) = \int U(\nu, \mathbf{r}) dr = \quad (12)$$

$$\frac{\sqrt{3}e^3}{mc^2} \int dr dE \frac{\nu}{\nu_c} \sin(2\chi) B_{\perp}(\mathbf{r}) f_e(E, \mathbf{r}) K_{2/3}\left(\frac{\nu}{\nu_c}\right)$$

where

$$\nu_c = \frac{3eB_{\perp}}{4\pi mc} \gamma^2 \quad (13)$$

and

$$\int dE d\Omega_E \cdot f_e(E, \mathbf{r}) = 4\pi \int dE \cdot f_e(E, \mathbf{r}) = n(\mathbf{r}). \quad (14)$$

In these equations, I , Q , and $U(\nu)$ are normalized so the radiation flux near Earth is given by $dF(\nu) = I(\nu)d\Omega = (dS/r^2)I(\nu)$ and so on, f_e is an isotropic electron distribution function, \mathbf{B}_{\perp} is a magnetic field projection to a plane transverse to the line-of-sight, and χ is the angle between the fixed direction in this plane and the main axis of the polarization ellipse. The parameters ν_c and χ are functions of \mathbf{r} .

Using the Stokes parameters, we obtain the degree of polarization as

$$\Pi(x, y) = \frac{\sqrt{U^2(x, y) + Q^2(x, y)}}{I(x, y)}, \quad (15)$$

where the coordinate system is shown in Fig. 3. We note that for large sources time delay is important and we take this into account with

$$\begin{pmatrix} I \\ Q \\ U \end{pmatrix} (x, y) = \int \begin{pmatrix} I \\ Q \\ U \end{pmatrix} \left(x, y, z, t - \frac{z}{c}\right) dz. \quad (16)$$

The main axis of the polarization ellipse of emitting synchrotron radiation is locally perpendicular to the magnetic field projection $B_{\perp}(\mathbf{r})$. If the rotation angle of polarization ellipse, χ , is measured from the $-Ox$ axis then $\cos \chi = B_{\perp y}/B_{\perp}$ and $\sin \chi = B_{\perp x}/B_{\perp}$, so

$$\tilde{Q}(\mathbf{r}, t, \nu) = S_c B_{\perp}(\mathbf{r}) K_{2/3}\left(\frac{\nu}{\nu_c}\right) \frac{B_{\perp y}^2 - B_{\perp x}^2}{B_{\perp}^2}, \quad (17)$$

$$\tilde{U}(\mathbf{r}, t, \nu) = S_c B_{\perp}(\mathbf{r}) K_{2/3}\left(\frac{\nu}{\nu_c}\right) \frac{2B_{\perp y} \cdot B_{\perp x}}{B_{\perp}^2}. \quad (18)$$

It is easily seen that in the case of isotropic turbulence $\langle \tilde{Q}(\mathbf{r}, t, \nu) \rangle = 0$ and $\langle \tilde{U}(\mathbf{r}, t, \nu) \rangle = 0$. In reality, the stochastic ensemble is not full so the average, while small, is not exactly zero. In the anisotropic case, if the axis of symmetry is perpendicular to the line-of-sight and coincides with axis Ox (or Oy) then the x and y field projections have different stochastic properties, i.e., $\langle B_{\perp y}^2 \rangle \neq \langle B_{\perp x}^2 \rangle$ and $\langle \tilde{Q}(\mathbf{r}, t, \nu) \rangle \neq 0$, while $\langle \tilde{U}(\mathbf{r}, t, \nu) \rangle = 0$. If $B_{\perp}^2/B_{\parallel}^2$ is large then $\langle \tilde{Q}(\mathbf{r}, t, \nu) \rangle$ can be close to the value for a homogeneous magnetic field and the polarization can be close to the maximum theoretical limit.

2.4. Electron distribution function

Due to rapid radiation losses, high-energy, shock accelerated electrons will be concentrated near the shock front. The characteristic width of this region is determined by the balance between the diffusive shock acceleration rate, diffusion out of the region, and the synchrotron loss rate. This width decreases rapidly with increasing electron energy making a plane-shock approximation reasonable. Following Bykov et al. (2000) we write the plane-shock diffusion-convection equation for DSA:

$$D(p) \frac{\partial^2 f_e}{\partial x^2} - u(x) \frac{\partial f_e}{\partial x} + \frac{p}{3} \frac{\partial u}{\partial x} \frac{\partial f_e}{\partial p} - \frac{1}{p^2} \frac{\partial}{\partial p} \left(p^2 \frac{dp}{dt} f_e \right) = 0 \quad (19)$$

where

$$\frac{dp}{dt} = -\frac{32\pi}{9} \left(\frac{e^2}{m_e c^2} \right)^2 \left(\frac{B^2}{8\pi} \right) \left(\frac{p}{m_e c} \right)^2 \quad (20)$$

describes synchrotron energy losses. For the plane-shock geometry, $f_e(E, \mathbf{r}) = f_e[E, d(\mathbf{r})]$, $\int f_e(E, \mathbf{r}) dE d\Omega_E =$

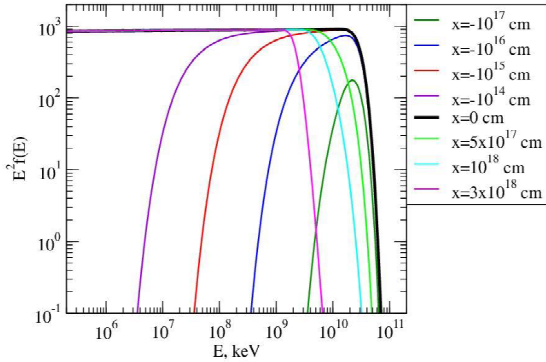


FIG. 2.— Electron distribution functions at different distances from the shock front as indicated. Negative values correspond to the upstream region while positive ones correspond to the downstream region.

$4\pi \int f_e(E, \mathbf{r}) dE = n(\mathbf{r})$, and $d = |\mathbf{r} - \mathbf{R}_0| - R_{\text{SNR}}$ is the distance to the shock front. Here, \mathbf{R}_0 is a radius-vector to the SNR center and R_{SNR} is SNR radius.

For our simulations we calculated synchrotron losses for a magnetic field $B = \sqrt{\langle B^2 \rangle} = 5.5 \cdot 10^{-5}$ G. This value is justified if the characteristic size of the magnetic field fluctuations is less than the average distance a particle moves during deceleration. The forward shock velocity used was $2 \cdot 10^8$ cm/s and we assumed Bohm diffusion. The model distribution functions of electrons are shown in Fig. 2. These electron distributions are generally consistent with standard DSA models where ultra-relativistic electrons and protons have the same spectral shape up to the break in the electron spectra due to synchrotron losses. While not shown, we find the associated proton distributions in the 100 GeV-TeV regime to be consistent with γ -ray spectra from Tycho's SNR as deduced from *Fermi* LAT and *VERITAS* observations (Archambault et al. 2017).

The spectra shown in Fig. 2 do not show effects from nonlinear shock modification produced by a strong CR pressure gradient in the shock precursor (e.g., Jones & Ellison 1991; Malkov & Drury 2001; Caprioli et al. 2011). Shock modification modifies the spectral shape and normalization of CR spectra including the high-energy end. The effect has been studied extensively for some young SNRs like RX J1713.7-3946 and Cas A (e.g., Ellison et al. 2012; Zirakashvili et al. 2014; Slane et al. 2015). However, the polarization results we present here are qualitatively similar with and without the nonlinear effects so we have used the unmodified spectra shown in Fig. 2.

2.5. Model SNR geometry

Tycho's SNR is among some young remnants having well developed small-scale structures in X-ray images. Here, we study the polarization properties of the magnetic turbulence believed associated with these structures in context of the new generation of X-ray polarimeters. We have simulated synchrotron intensity and polariza-

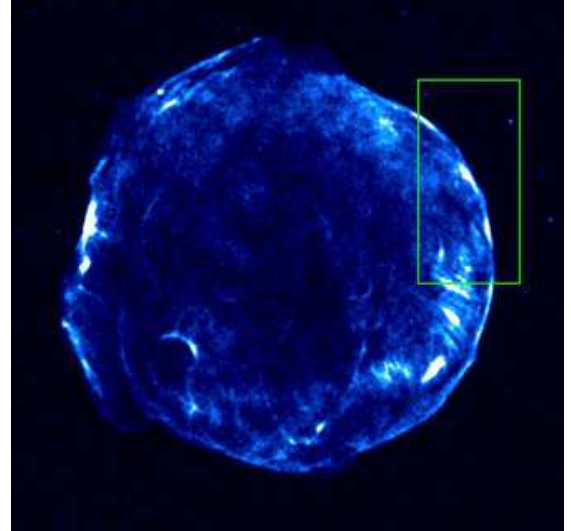
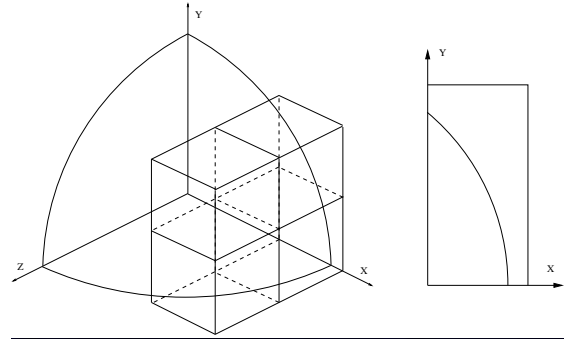


FIG. 3.— The model geometry is shown in the top left where 4 of the 8 simulation boxes are shown. One-eighth of the spherical SNR shock is indicated along with the coordinate axes and, on the right, a schematic 2D image obtained after an integration over the line-of-sight. The Oz axis is directed to the observer. The bottom panel shows the 6–8 keV *Chandra* image of Tycho's SNR with the location of a 120×240 arcsec rectangular region which is equal in size to our model region used in simulations in Section 3.

tion maps of a Tycho-like SNR in X-ray energies taking into account stochastic properties of the magnetic field. We assume a remnant radius of 3 pc, at a distance of 2.5 kpc, giving an angular radius of to 4 arcmin.⁷

We simulated magnetic fields in a rectangular box with dimensions $(16 \times 8 \times 4) \cdot 10^{18}$ cm, consisting of eight cubes with sides $D = 4 \cdot 10^{18}$ cm. As shown in Fig. 3, this box contains a part of the SNR shell. Our minimal and maximal scales of turbulence are $L_{\text{min}} \sim 2.5 \cdot 10^{15}$ cm and $L_{\text{max}} \sim 1.2 \cdot 10^{18}$ cm. In angular units this is $L_{\text{min}} \sim 0.07$ arcsec and $L_{\text{max}} \sim 30$ arcsec. We calculated Stokes parameters of the synchrotron emission in this volume for different models of isotropic and anisotropic magnetic turbulence both with $\sqrt{\langle B^2 \rangle} = 5.5 \cdot 10^{-5}$ G.

After integration over the line-of-sight (OZ axis in Fig. 3) we obtained 2D intensity and polarization maps

⁷ We note that 2.5 kpc is at the low end of generally cited distances for Tycho's SNR which can be 3 kpc or a bit higher (e.g., Slane et al. 2015; Sato & Hughes 2017).

of the synchrotron radiation. We used 2000 pixels along the line-of-sight and 100x100 pixels in a transverse plane in each cubic box. On the right panel of Fig. 3 the 120×240 arcsec simulated rectangular region is shown superimposed on the Tycho's SNR *Chandra* image.

We simulated the axially symmetric magnetic turbulence with an axis of symmetry directed along the Ox axis while the real symmetry of the system is spherical. Our simulation results are precise at the part of the SNR shell normal to the Ox axis ($y=0$) and accurate enough for our simulation maps in nearby regions.

3. MAGNETIC TURBULENCE AND SNR SYNCHROTRON IMAGES

3.1. Ideal observations

Here we discuss ‘ideal’ observations, i.e., ones with long enough exposures so all statistically uncertainties are negligible for every pixel. We do not, however, assume infinite angular resolution. This ideal case allows us to identify synchrotron emission properties of young SNRs and serves as a starting point for simulations of real synchrotron images taking into account polarimeter sensitivity, effective area, limited exposure, and Poisson photon statistic. These realistic simulations are discussed in Section 3.2.

Based on the model described above we simulated synchrotron maps for Stokes parameters I , U , and Q assuming an angular resolution of 1.2 arcsec. This allows us to obtain maps of the intensity, polarization degree, and polarization angle with the same or worse resolution of the forthcoming *IXPE* X-ray polarimeter (see Weisskopf et al. 2016).

We simulated cases with isotropic and anisotropic magnetic turbulence. For the isotropic case, we used magnetic field fluctuations with power spectrum indices $\delta = 5/3$ and $\delta = 1$. In the anisotropic case, we consider both turbulence produced due to shock compression and due to anisotropic cascading. In the shock compression case, we consider magnetic turbulence with power spectrum index $\delta = 5/3$ and strength of anisotropy $q = 5$ and 20. Radiation maps obtained in these cases for a photon energy of 5 keV are shown in Fig. 4 with 1.2 arcsec angular resolution. The dependence on the spectral index is clearly seen in the relative sizes of magnetic structures in the high resolution intensity and polarization images for different values of δ . It is also seen that stronger anisotropy (greater q) in shock compression turbulence results in stronger polarization with mostly a radial polarization direction.

This agrees well with the fact that the polarization in highly anisotropic turbulence approaches the maximum theoretical limit of polarization in a homogeneous magnetic field. The main difference comes about because, for a homogeneous magnetic field, the total emission from the entire SNR is highly polarized. For anisotropic turbulence, only small scale structures are highly polarized and the total emission is not significantly polarized because contributions from different parts of the remnant cancel each other on average.

In Fig. 5 we show maps of the quantities from

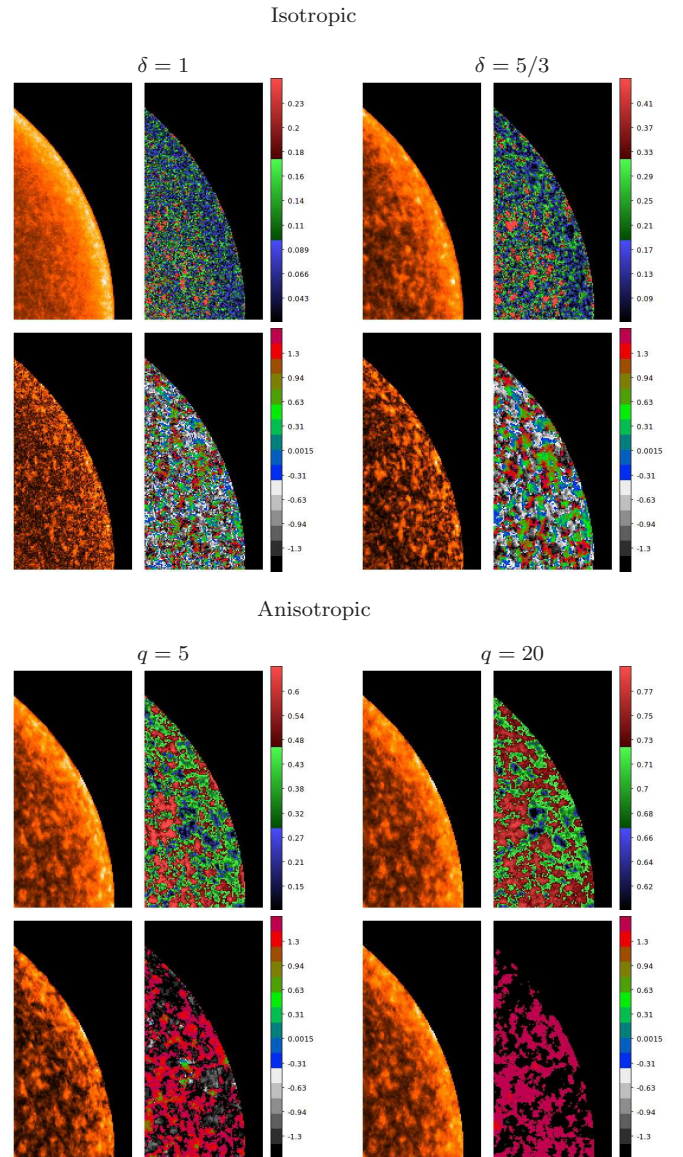


FIG. 4.— Model synchrotron images with 1.2'' angular resolution. In each of the 4 sections, the total emission is in the upper left, the polarized emission is in the lower left, the polarization degree is in the upper right and the polarization angle (in radians) is in the lower right. Angles are measured from the Oy axis. The left and right panels in the first row, respectively, show isotropic turbulence examples for turbulence power spectra indices $\delta=1$ and $5/3$. The left and right panels in the bottom row, respectively, show anisotropic turbulence cases with $\delta=5/3$ and $q = 5$ and 20.

Fig. 4 with the expected angular resolution of the *IXPE* polarimeter as a convolution with PSF taken from (Fabiani et al. 2014). The work of Fabiani et al. (2014) describes the PSF of the *IXPE* polarimeter and we assume this is similar to the PSF of *IXPE*. The PSF was truncated to a circle with 36 arcsec radius in order to decrease the influence of border effects. In the maps shown in Fig. 5, the *IXPE* PSF width exceeds the smallest scale structures so, after convolution, these structures will become much less prominent. Nevertheless, there

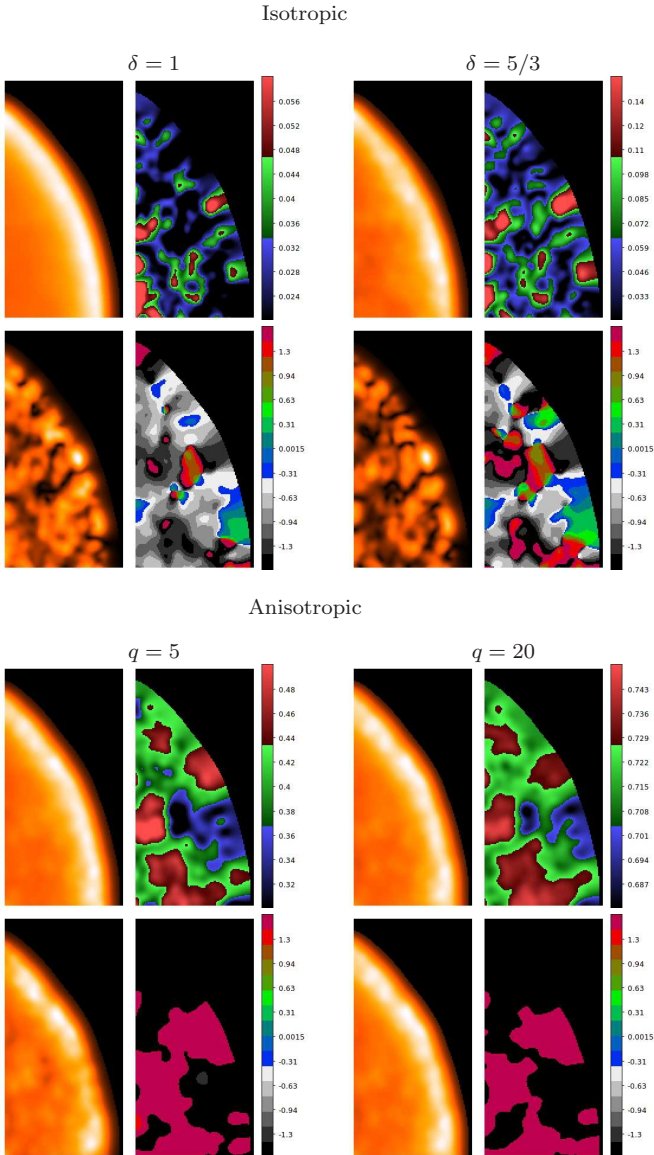


FIG. 5.— Model synchrotron images obtained after convolution with the *IXPE* PSF are shown. In each of the 4 sections, the total emission is in the upper left, the polarized emission is in the lower left, the polarization degree is in the upper right, and the polarization angle (in radians) is in the lower right. Angles are measured from the O_y axis. The left and right panels in the top row, respectively, show isotropic turbulence examples for turbulence power spectra indices $\delta = 1$ and $5/3$. The left and right panels in the bottom row, respectively, show anisotropic turbulence examples with $\delta = 5/3$ and $q = 5$ and 20 .

is a difference in polarization between the homogeneous and anisotropic cases after convolution so future X-ray polarimeters could give quantitative information on the level of anisotropic magnetic turbulence in SNRs.

To model turbulent magnetic field produced in a cascading process we used power spectra of weak turbulence cascade as described in Section 2.1. The stochastic field properties correspond to $q = 1.05$. If no large-scale homogeneous field is present, this stochastic field

alone can be used to model strong turbulence cascade. Weak turbulence can be modeled with the addition of a large-scale homogeneous field in which case the strength of turbulence depends on the ratio between B_{hom}^2 and $\langle B_{\text{tur}}^2 \rangle$. In all of our examples, we fix the value of $\langle \mathbf{B}^2 \rangle = \langle (\mathbf{B}_{\text{hom}} + \mathbf{B}_{\text{tur}})^2 \rangle = \text{const}$, an important factor for electron diffusion and energy losses. We chose a direction of the large-scale magnetic field, which is also the symmetry axis, along the axis O_x . In the model geometry (Fig. 3), this direction mimics a radially directed large-scale magnetic field.

Fig. 6 shows synchrotron images for these turbulent fields. It can be seen that, while radiation is more polarized for weaker turbulence, there remains significant polarization for strong turbulence. In both cases, the most likely direction of polarization is along the O_y axis, i.e., tangent to the shock front. This direction differs from the one for turbulence produced by shock compression. This result remains after convolution with the *IXPE* PSF making it possible to distinguish anisotropic cascade turbulence from shock compressed turbulence.

3.2. Simulation of realistic *IXPE* observations

Realistic simulations of the X-ray band should take into account the detector sensitivity and the Poisson statistics of the incoming photons. Supernova remnants are extended objects so even if the entire remnant is a strong source, spatially resolved parts are likely to be rather weak sources. In Weisskopf et al. (2010) it is stated that detection of polarization requires much better statistics than needed for spectral analysis. With this in mind, we explore the requirements to detect and study the polarization properties of Tycho's SNR by the forthcoming *IXPE* polarimeter.

For our simulations we have used the publicly available XIMPOL code⁸ with the high resolution maps discussed above as sources. For the electron flux we used an XSPEC power law model with spectral index 2.2 and normalization $1.2 \cdot 10^{-2}$ ph/keV/cm²/s at 1 keV. These numbers result from the spectral fitting of the *Chandra* flux from the box region shown in the *Chandra* image in Fig. 3. To account for the unpolarized thermal emission from the SNR, we reduced the model polarization degree by the ratio of the observed synchrotron flux to the total flux. This ratio was determined by fitting joint thermal/nonthermal models to spectra obtained from *Chandra* observations of Tycho. The models provide only modest representations of the complex X-ray spectra from the different regions, but yield reasonable estimates for the thermal and nonthermal flux. Maps of the ratio of the synchrotron flux to the total flux are shown in Fig. 8 for the indicated energy bands. To decrease the influence of the thermal plasma, we model 3–8 keV radiation for which the fraction of thermal plasma emission near the ridge is ~ 0.2 .

Figure 7 shows the results of the XIMPOL simulation for anisotropic turbulence produced by shock compression and shown in Fig. 4 for $q = 5$ and a total exposure of

⁸ <https://github.com/lucabaldini/ximpol>

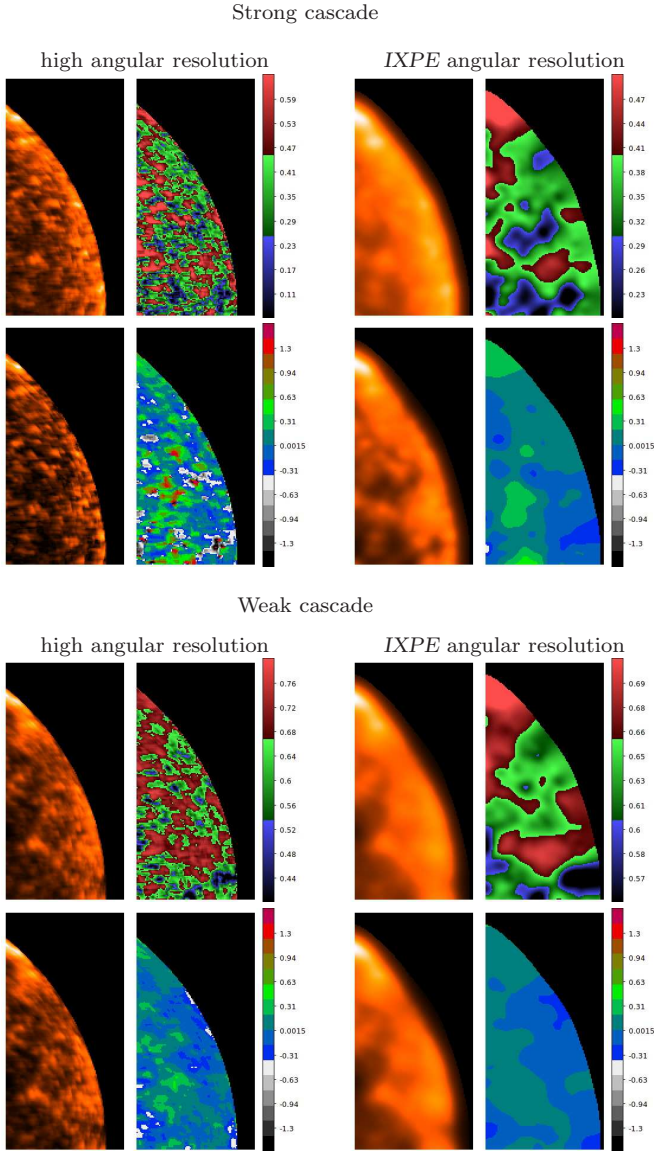


FIG. 6.— These images were generated with turbulence produced in an anisotropic cascade process. In each panel the total emission is in the upper left, the polarized emission is in the lower left, the polarization degree is in the upper right, and the polarization angle (in radians) is in the lower right. Angles are measured from the Oy axis. Images with angular resolution $1.2''$ are in the left column and images obtained after convolution with *IXPE* PSF are in the right column. The first row shows the case of anisotropic turbulence produced in the strong anisotropic cascade model with $q = 1.05$. The second row shows the case of anisotropic turbulence produced in the weak anisotropic cascade model (see text).

1 Ms. The upper panel shows the results using 1 arcmin size pixels within the image. Highly significant polarization is detected in one region, with lower significance obtained in one other region. The measured polarization angle for these regions is consistent with that for the large-scale structures in Fig. 4, while the polarization degree is somewhat lower, as expected from the contributions of small disorganized regions.

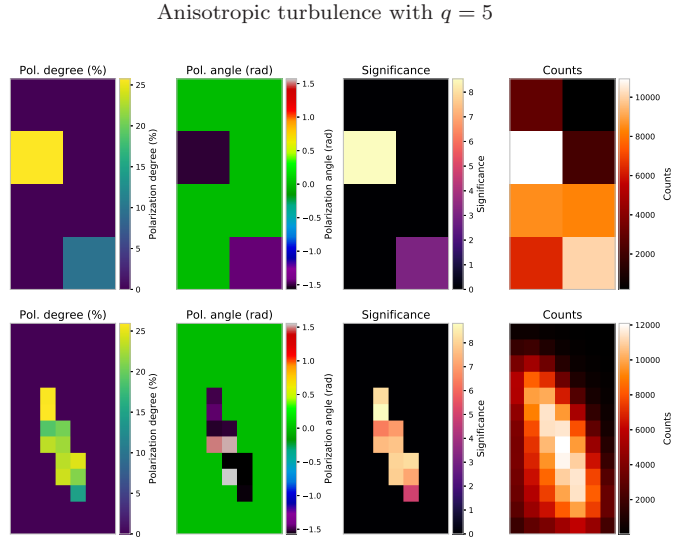


FIG. 7.— Top and bottom panels show XIMPOL simulated maps for the case of anisotropic turbulence produced by shock compression with $q = 5$ and $\delta = 5/3$. The upper panels show maps with pixel size equal to the region from which statistics were collected. The lower panels were obtained for the dense grid with pixel size smaller than the size of the circular region that was used to collect statistics (“sliding circle” approach). Each row shows maps of polarization degree, angle, significance, and total counts. The maps of polarization degree, angle, and significance show only pixels with collected statistics better than 10,000 counts.

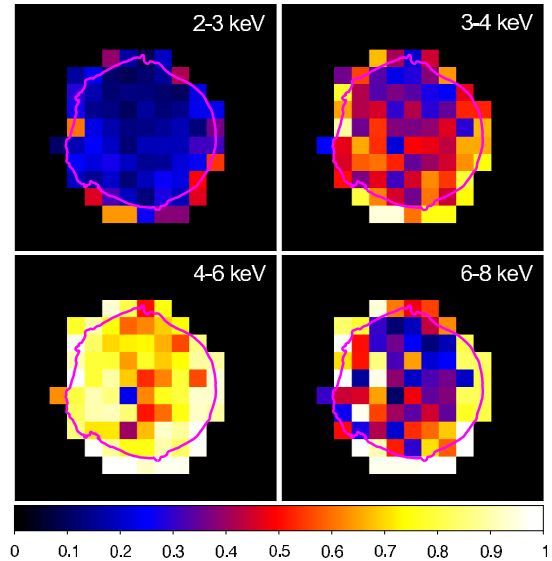


FIG. 8.— Ratio maps of the synchrotron flux to total flux for Tycho’s SNR. Values from these maps were used to approximate the ratio of polarized to unpolarized flux for the region in Fig. 3 being considered for simulations presented here. The outermost contour from the Chandra image of Tycho is shown for reference.

To investigate spatial variations in the polarization, we have adopted a “sliding circle” approach wherein we use a dense grid with ≈ 17.5 arcsec size pixels and obtain statistics from a 30-arcsec radius circle centered on the pixel. Each pixel thus shows a numerical value that actually corresponds to counts from a larger surrounding region. We show only pixels with greater than 10,000 counts, sufficient to detect $\sim 10\%$ polarization with 99% c.l. (with a detector modulation factor 0.5 and without background (Weisskopf et al. 2010)).

The dense grid, while showing pixel-to-pixel values that are not statistically independent (and do not correspond to the small pixel size), provides an important guide to the source structure. This is particularly true for the sharp border of the SNR, where an arbitrary large region used for extracting X-ray events may fail to yield sufficient counts to detect the polarization along the rim. As can be seen from comparison with Fig. 4, the sliding-circle maps provide a more faithful representation of the input model for the simulations. For a more complete analysis, a tessellation scheme that samples the image so as to obtain sufficient counts to probe the polarization structure could be employed. This is beyond the scope of our investigation here, which is aimed at demonstrating broad sensitivity to the turbulence models described above. The *IXPE* field of view is $\sim 10''$ in diameter, sufficiently large for single pointings to encompass many SNRs in their entirety, including Cas A and Tycho’s SNR. Based on the results from the upper panel, we conclude that, under the assumptions of the associated turbulence model, a ~ 1 Ms *IXPE* observation of Tycho would yield ~ 15 discrete regions from the entire SNR for which high-significance polarization detections would result.

Figure 9 shows XIMPOL simulations for anisotropic cascade produced turbulence again assuming a 1 Ms *IXPE* observation. Comparing Figs. 7 and 9 shows that it is possible to distinguish anisotropic cascade turbulence from shock compressed turbulence by the direction of polarization. Indeed ? obtained that a 1σ angle error in a polarization angle measurement is $\sim 28.5/\beta$ deg, where $\beta = a/\sigma_a$, a is the polarization amplitude, and σ_a is the 1σ polarization amplitude error. The significance value that is plotted in Figs. 7 and 9 is also equal to a/σ_a . Our simulations show that in some cases of the anisotropic magnetic turbulence we should detect polarization with significance ~ 8 or even greater from ~ 15 regions along the Tycho SNR shell. This would suggest that it is possible to obtain ~ 10 degree, 3σ accuracy for these regions that is sufficient to distinguish the cases of radial, tangential, and intermediate polarization directions one from another.

In the area near the SNR blast wave the situation is as follows: for turbulence produced by anisotropic cascade the assumed direction of the magnetic field is along the SNR radius and the direction of polarization is tangential to the SNR shock. For turbulence produced by shock compression, the dominant magnetic field direction will be in the shock plane making the dominant direction of polarization along the SNR radius. For

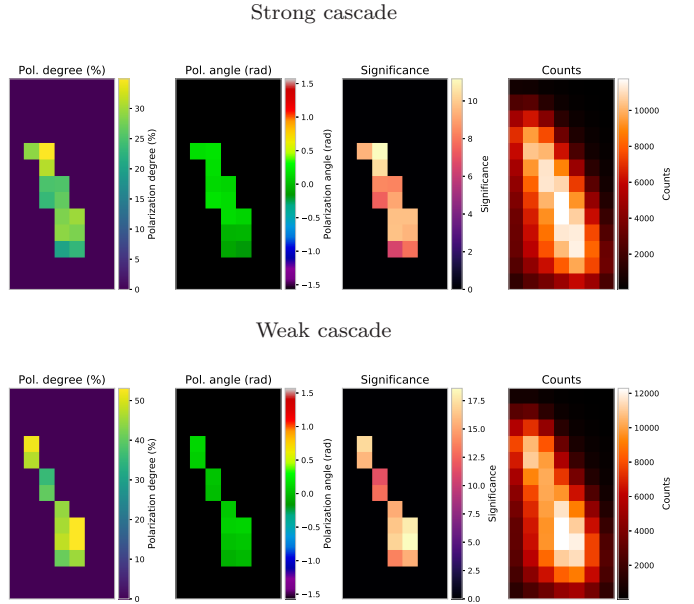


FIG. 9.— The upper panels show the XIMPOL simulated maps for a strong cascade case (upper row of Fig. 6) and the lower panels show the same maps for the weak cascade case (lower row of Fig. 6). Shown are the polarization degree, angle, significance, and total counts (intensity) for pixels with collected statistics greater than 10,000 counts. All panels are for the dense grid with pixel size smaller than the circular region that was used to collect statistics.

isotropic turbulence (i.e., isotropic cascade) it is not possible to detect significant polarization with a 1 Ms exposure. The XIMPOL simulations are not shown for this case.

4. CONCLUSIONS

The stochastic properties of magnetic turbulence leave observational traces in the small-scale structure of synchrotron X-ray intensity and polarization maps of astrophysical objects. In SNR images this structure is manifested as clumps, dots, and filaments. It is sensitive to the map energy band, to the underlying electron spectrum, and to the level of anisotropy of the magnetic turbulence. Due to the characteristics of DSA in young SNRs, the X-ray synchrotron energy band is the most sensitive band to study this effect.

When properly analyzed, polarization effects can provide additional information on the X-ray synchrotron structure beyond that obtained from synchrotron intensity maps alone. It is important that, for certain types of magnetic turbulence, some features in the images of polarization degree and angle remain even with the low angular resolution of 20–30 arcsec expected from the current generation of X-ray polarimeters.

In this article we have discussed the difference in the X-ray synchrotron map structures that emerge in the cases of anisotropic turbulence produced by shock compression and by cascading processes. Our results, simulating observations of $\sim 1/8$ th of Tycho’s SNR, suggest that a 1 Ms *IXPE* observation will have sufficient sensitivity to yield highly-significant polarization

detections in multiple discrete regions around the entire SNR boundary. If strong turbulence is short-scale and isotropic upstream of the outer blast wave, we will see mostly radial polarization in the downstream region after shock compression. However, if isotropic cascading occurs downstream, small-scale domains will form with random magnetic field directions and polarization that is undetectable with a 1 Ms *IXPE* observation. We note that, during testing of the radial (or tangential) polarization model, polarization angles around the entire periphery of the SNR can be re-phased to greatly increase the sensitivity of the measurements.

On the other hand, if CRs are accelerated at the forward shock efficiently enough to have a hard spectrum (i.e., an index of 2 or less at the highest energies indicative of nonlinear DSA) then we can expect to have strong long-wavelength fluctuations of spatial scales up to 10 arcsec in Tycho. Also, the long-wavelength magnetic structures could be produced by the non-resonant CR mirror instability which may indicate the superdiffusive regime of CRs acceleration by supernova shocks (Bykov et al. 2017). Since the lifetime of large-scale fluctuations is of the order of a few years or longer, the dominant magnetic field seen by a snapshot will be a random combination of patches of quasi-regular strong fields. Within the anisotropic cascade model, when the magnetic field near the shock is predominantly radial, this pattern will produce polarization that is predomi-

nantly parallel to the shock front and distinct from the case of shock compressed turbulence.

Of course this picture is oversimplified since we are only considering the forward shock and projection effects, even for the forward shock, will tend to obscure the polarization direction. A clear prediction, however, comes from the expected timescale for magnetic fluctuations. If *IXPE* observes Tycho twice within more than a ten-year interval, significant changes in the polarization are expected from the anisotropic cascade, CR-driven turbulence models.

We have described features detectable with the new generation of X-ray polarimeters such as *IXPE*. These detectors should give unique and valuable information on the properties of magnetic turbulence including its origin and evolution in SNRs.

5. ACKNOWLEDGMENTS

The authors thank the anonymous referee for a careful reading of our paper and constructive comments. Most calculations were done on computers of the RAS JSCC and St-Petersburg department of the RAS JSCC and at the Tornado subsystem of the St. Petersburg Polytechnic University supercomputing center. AMB was supported by the RSF grant 16-12-10225. PS acknowledges partial support from NASA contract NAS8-03060.

REFERENCES

- Alfvén, H. & Herlofson, N. 1950, *Physical Review*, 78, 616
- Amato, E. 2014, *International Journal of Modern Physics D*, 23, 1430013
- Amato, E. & Blasi, P. 2006, *MNRAS*, 371, 1251
- Archambault, S., Archer, A., Benbow, W., et al. 2017, *ApJ*, 836, 23
- Axford, W. I. 1981, in *IAU Symposium*, Vol. 94, *Origin of Cosmic Rays*, ed. G. Setti, G. Spada, & A. W. Wolfendale, 339–358
- Baade, W. & Zwicky, F. 1934, *Phys. Rev.*, 46, 76
- Bamba, A., Yamazaki, R., Yoshida, T., Terasawa, T., & Koyama, K. 2005, *ApJ*, 621, 793
- Bandiera, R. & Petruk, O. 2016, *MNRAS*, 459, 178
- Bell, A. R. 2004, *MNRAS*, 353, 550
- Bell, A. R., Gull, S. F., & Kenderdine, S. 1975, *Nature*, 257, 463
- Bigot, B., Galtier, S., & Politano, H. 2008, *Phys. Rev. E*, 78, 066301
- Blandford, R. & Eichler, D. 1987, *Physics Reports*, 154, 1
- Bykov, A. M., Brandenburg, A., Malkov, M. A., & Osipov, S. M. 2013, *Space Sci. Rev.*, 178, 201
- Bykov, A. M., Chevalier, R. A., Ellison, D. C., & Uvarov, Y. A. 2000, *ApJ*, 538, 203
- Bykov, A. M., Ellison, D. C., & Osipov, S. M. 2017, *Phys. Rev. E*, 95, 033207
- Bykov, A. M., Ellison, D. C., Osipov, S. M., & Vladimirov, A. E. 2014, *ApJ*, 789, 137
- Bykov, A. M., Uvarov, Y. A., Bloemen, J. B. G. M., den Herder, J. W., & Kaastra, J. S. 2009, *MNRAS*, 399, 1119
- Bykov, A. M., Uvarov, Y. A., & Ellison, D. C. 2008, *ApJ*, 689, L133
- Caprioli, D., Blasi, P., & Amato, E. 2011, *Astropart. Phys.*, 34, 447
- Chevalier, R. A. 1977, *ARA&A*, 15, 175
- Cho, J., Lazarian, A., & Vishniac, E. T. 2002, *ApJ*, 564, 291
- Dickel, J. R., van Breugel, W. J. M., & Strom, R. G. 1991, *AJ*, 101, 2151
- Dubner, G. & Giacani, E. 2015, *A&A Rev.*, 23, 3
- Duin, R. M. & Strom, R. G. 1975, *Astronomy and Astrophysics*, 39, 33
- Ellison, D. C., Slane, P., Patnaude, D. J., & Bykov, A. M. 2012, *ApJ*, 744, 39
- Eriksen, K. A., Hughes, J. P., Badenes, C., et al. 2011, *ApJ*, 728, L28+
- Fabiani, S., Costa, E., Del Monte, E., et al. 2014, *ApJS*, 212, 25
- Fürst, E. & Reich, W. 2004, in *The Magnetized Interstellar Medium*, ed. B. Uyaniker, W. Reich, & R. Wielebinski, 141–146
- Giacalone, J. & Jokipii, J. R. 1999, *ApJ*, 520, 204
- Ginzburg, V. L. & Syrovatskii, S. I. 1964, *The Origin of Cosmic Rays*, New York: Macmillan
- Ginzburg, V. L. & Syrovatskii, S. I. 1965, *Annual Review of Astronomy and Astrophysics*, 3, 297
- Goldreich, P. & Sridhar, S. 1997, *ApJ*, 485, 680
- Helder, E. A., Vink, J., Bykov, A. M., et al. 2012, *Space Sci. Rev.*, 173, 369
- Jones, F. C. & Ellison, D. C. 1991, *Space Science Reviews*, 58, 259
- Jun, B.-I. & Norman, M. L. 1996, *ApJ*, 465, 800
- Lazendic, J. S., Slane, P. O., Gaensler, B. M., et al. 2004, *ApJ*, 602, 271
- Lee, H., Cho, J., & Lazarian, A. 2019, *ApJ*, 877, 108
- Lithwick, Y. & Goldreich, P. 2003, *ApJ*, 582, 1220
- Malkov, M. A. & Drury, L. 2001, *Reports of Progress in Physics*, 64, 429
- Marcowith, A., Bret, A., Bykov, A., et al. 2016, *Rep. Progr. Phys.*, 79, 046901
- Okuno, T., Tanaka, T., Uchida, H., et al. 2020, *arXiv e-prints*, arXiv:2003.10035
- Parizot, E., Marcowith, A., Ballet, J., & Gallant, Y. A. 2006, *Astronomy and Astrophysics*, 453, 387
- Patnaude, D. J. & Fesen, R. A. 2009, *ApJ*, 697, 535
- Petruk, O., Bandiera, R., Beshley, V., Orlando, S., & Miceli, M. 2017, *MNRAS*, 470, 1156
- Pohl, M., Yan, H., & Lazarian, A. 2005, *ApJ*, 626, L101
- Raymond, J. C. 1984, *ARA&A*, 22, 75

- Reville, B., O'Sullivan, S., Duffy, P., & Kirk, J. G. 2008, MNRAS, 386, 509
- Reynolds, S. P. 2008, ARA&A, 46, 89
- Reynolds, S. P. & Chevalier, R. A. 1981, ApJ, 245, 912
- Reynolds, S. P., Gaensler, B. M., & Bocchino, F. 2012, Space Sci. Rev., 166, 231
- Reynoso, E. M., Moffett, D. A., Goss, W. M., et al. 1997, ApJ, 491, 816
- Sato, T. & Hughes, J. P. 2017, ApJ, 840, 112
- Schure, K. M., Bell, A. R., O'C Drury, L., & Bykov, A. M. 2012, Space Sci. Rev., 173, 491
- Shebalin, J. V., Matthaeus, W. H., & Montgomery, D. 1983, Journal of Plasma Physics, 29, 525
- Slane, P., Lee, S.-H., Ellison, D. C., et al. 2015, ApJ, 799, 238
- Sridhar, S. & Goldreich, P. 1994, ApJ, 432, 612
- Strom, R. G. & Duin, R. M. 1973, Astronomy and Astrophysics, 25, 351
- Uchiyama, Y. & Aharonian, F. A. 2008, ApJ, 677, L105
- Uchiyama, Y., Aharonian, F. A., Tanaka, T., Takahashi, T., & Maeda, Y. 2007, Nature, 449, 576
- Vink, J. 2012, A&A Rev., 20, 49
- Vink, J. & Laming, J. M. 2003, ApJ, 584, 758
- Wang, R.-Y., Zhang, J.-F., & Xiang, F.-Y. 2020, ApJ, 890, 70
- Weisskopf, M. C., Elsner, R. F., & O'Dell, S. L. 2010, Society of Photo-Optical Instrumentation Engineers (SPIE) Conference Series, Vol. 7732, On understanding the figures of merit for detection and measurement of x-ray polarization, 77320E
- Weisskopf, M. C., Ramsey, B., O'Dell, S., et al. 2016, in Proc. SPIE, Vol. 9905, Space Telescopes and Instrumentation 2016: Ultraviolet to Gamma Ray, 990517
- West, J. L., Jaffe, T., Ferrand, G., Safi-Harb, S., & Gaensler, B. M. 2017, ApJ, 849, L22
- Zirakashvili, V. N., Aharonian, F. A., Yang, R., Oña-Wilhelmi, E., & Tuffs, R. J. 2014, ApJ, 785, 130